Alumina based ceramics for high-voltage insulation

Matthieu Touzin, Dominique Goeuriot, Christelle Guerret-Piecourt, Denyse
Juvé, Hans-Joachim Fitting

Alumina based ceramics for high-voltage insulation

M. Touzin [a], D. Goeuriot [b,*], C. Guerret-Piécourt [c], D. Juvé [c], H.-J. Fitting [d]

a Laboratoire de Structure et Propriétés de l'Etat Solide, UMR CNRS 8008, Université de Lille 1, 59655 Villeneuve d'Ascq, France
b Centre Sciences des Matériaux et des Structures, UMR CNRS 5146, Ecole Nationale Supérieure des Mines, 158 cours Fauriel, F-42023 Saint-Etienne Cedex 2, France
c Laboratoire de Tribologie et Dynamique des Systèmes, Ecole Centrale de Lyon, UMR CNRS 5513, 36 avenue Guy de Collongue, F-69134 Ecully Cedex, France
d Physics Department, University of Rostock, Universitätsplatz 3, D-18051 Rostock, Germany

Abstract

Dielectric breakdown constitutes an important limitation in the use of insulating materials under high-voltage since it can lead to the local fusion and sublimation of the insulator. The role of electrical charge transport and trapping in alumina ceramics on their resistance to this catastrophic phenomenon is studied in this work. In polycrystalline materials, the interfaces between the various phases play a main role because they constitute potential sites for the trapping of electrical charges. The density and the nature of these interfaces can be controlled by the way of the microstructure parameters. So, the aim of the present paper is to highlight the influence of average grain size and intergranular phase crystallization rate on the ability of polycrystalline alumina materials to resist to dielectric breakdown. Thus, it is shown that the control of the process conditions (sintering aids content, powder grain size and thermal cycle) makes it possible to change not only the density (by the average grain size) but also the nature (by the crystallization or not of anorthite) of the grain boundaries. On one hand, at room temperature a high density of interfaces, due to low grain size and highly crystallized intergranular phase, leads to a high dielectric strength. On the other hand, at higher temperature (250 °C), the presence of vitreous intergranular phase makes it possible to delay breakdown. That behaviour is explained thanks to charge transport and trapping characterizations.

---

* Corresponding author.
E-mail address: dgoeurio@emse.fr (D. Goeuriot).

1. Introduction

Ceramic insulator materials are widely used for high-voltage applications. One of the main limitations in this kind of use is the risk of dielectric breakdown that leads to the irreversible degradation of the material. Breakdown phenomenon can be attributed to the sudden and rough destabilisation of the charges accumulated in the material during e-injection. Indeed, when charges are injected into an insulator by electronic irradiation or by applying an electric voltage, they and those generated by electron–hole pair creation can be trapped in specific sites. This charge localisation induces a polarization and then a deformation of the lattice allowing the accumulation of a great amount of energy into the material.[1] The sudden destabilisation of charges by the way of an electrical, mechanical or thermal perturbation will lead to the release of the stored energy. Then it is reasonable to assume that the ability of a material to resist high-voltage conditions without reaching breakdown is directly linked to its charge trapping and scattering properties.[2,3] Of course, these properties depend on the material microstructure[4,5] and in particular on the interfaces. Indeed, grain boundaries, i.e. interfaces between different phases, are numerous in ceramics and constitute sites for the trapping of electric charges.[6] In this paper, we propose some correlations between the elaboration conditions, the microstructure (in terms of interface density and nature), the charge trapping properties and the dielectric strength for liquid phase sintering polycrystalline alumina materials.

In the first part of this study, relationships are established between the process conditions and the final property: dielectric breakdown resistance E_b, using a polynomial model. Four parameters were considered: powder grain size, sintering aids amount (CaO, SiO$_2$, MgO) and sintering time and temperature. Then, E_b obtained for a panel of materials are explained considering microstructure parameters, mainly grain size and intergranular phase. Charge transport measurements are performed thanks to an instrumented Scanning Electron Microscope (Induced Current Method and Scanning Electron Microscopy Mirror Effect) in order to interpret those results. Finally some explanations on the reactions occurring in this system during sintering are given, that permit the control of the intergranular crystallization in order to optimize the dielectric strength.

2. Materials and experimental procedure

2.1. Material processing

The starting powders were prepared from commercial alumina powders mixed with various amounts of sintering aids (CaO, SiO$_2$, MgO) in water. Because of proprietary constraints, we will not name the exact mineral additives used but the total corresponding oxide amount. Their content was from 3.64

to 7.89 wt.% (with a constant MgO:CaO:SiO$_2$ weight ratio 1:1.35:2.65). In some cases, to reduce the average particle size, the powder was also milled by attrition using 0.4 mm diameter CeO$_2$ stabilised zirconia balls for 15 or 30 min. On the whole, thirty different materials were prepared. For material 29, a smaller grain sized alumina powder was used. Binders were also incorporated in the slurry. The powders were then spray-dried. Table 1 presents the characteristics of these powders.

Pressed samples were obtained by uniaxial compression under 30 MPa in order to form pellets of 20 mm in diameter. Debinding was performed at 600 °C for 2 h. Open air sintering was carried out within a temperature range from 1540 to 1630 °C for various soaking times (from 45 up to 120 min). The heating rate for the sintering treatment was 150 °C/h. The initial cooling rate was 78 °C/h which increased to 150 °C/h when temperature fell below 1400 °C. Elaboration parameters for the different materials are summarized in Table 2.

2.2. Characterizations

2.2.1. Structural characterizations

The density of the sintered samples was measured by the water-immersion method (Archimedes). Microstructures were studied by Scanning Electron Microscopy (JEOL JSM840) and Transmission Electron Microscopy (PHILIPS CM200). The average grain size was obtained by the intercept method on SEM micrographs of polished surfaces which were thermally etched 20 min at 1460 °C. The porosity was evaluated by back-scattered electron micrograph analysis performed on fracture faces. Intergranular phase composition was analysed by X-ray diffraction. Quantifications from XRD patterns are based on the peaks surface areas: (1 0 4) peak for the quantification of α-alumina, (3 1 1) peak for spinel MgAl$_2$O$_4$ and (0 4 0), (2 0 −4) and (0 0 4) peaks (without deconvolution) for anorthite phase CaAl$_2$Si$_2$0$_8$, which were the detected phases in the sintered samples. Considering the initial composition for the four oxides (Al$_2$O$_3$, CaO, MgO and SiO$_2$), it is possible to theoretically calculate the percentage of the three different phases observed after sintering: Al$_2$O$_3$, MgAl$_2$O$_4$ and CaAl$_2$Si$_2$O$_8$; it is assumed that all of the available oxides derived from the additives is consumed to form the different phases (only a little CaO leftover: it can be noted

Table 1
Starting powder characteristics.

Milling time (min)	Max (μm)[a]	d_{10} (μm)[b]	d_{90} (μm)[c]
0	3.1	1.1	6.1
15	3.0	1.1	6.3
30	2.5	0.9	4.7
Fine alumina	1.7	0.7	6.7

[a] Diameter for the highest number of grains.
[b] 10% of grains in number have a lower diameter.
[c] 90% of grains in number have a lower diameter.

Table 2
Elaboration parameters, microstructural parameters and dielectric strength E_b at 25 °C of the materials prepared for this study ((*) use of fine alumina, see Table 1).

Reference	Milling time (min)	Sintering additives (%)	Sintering conditions		Intergranular crystallization rate (%)		Glass coefficient $\Delta\alpha$	Average grain diameter (μm)	Porosity (%)	E_b (25 °C) (kV/mm)
			Time (min)	T (°C)	$X_{\text{anorthite}}$	X_{spinel}				
1	15	4.13	90	1585	0	77.4	6.4	2.1	4.4	14.3 ± 0.4
2	15	5.10	90	1585	0	78.9	8.0	2.3	3.1	14.5 ± 0.8
3	15	3.14	90	1585	0	73.0	4.8	2.1	3.7	14.3 ± 0.6
4	15	4.62	135	1585	0	60.7	8.0	3.4	3.0	14.3 ± 0.4
5	15	3.64	45	1585	–	–	–	1.9	3.0	14.2 ± 0.9
6	15	4.62	45	1585	–	–	–	2.1	3.3	14.2 ± 0.9
7	15	3.62	135	1585	–	–	–	2.5	3.7	14.3 ± 0.6
8	15	4.62	105	1630	0	80.9	7.1	4.4	3.0	13.7 ± 0.5
9	15	3.64	75	1540	–	–	–	1.8	5.3	12.0 ± 2.6
10	15	4.62	75	1540	–	–	–	1.8	5.6	13.3 ± 0.8
11	15	4.13	120	1540	90.7	100.0	0.5	1.8	4.9	14.0 ± 0.9
12	15	3.64	105	1630	0	62.5	6.0	3.6	2.9	13.6 ± 0.6
13	15	4.13	60	1630	0	96.8	5.8	3.2	3.7	13.9 ± 0.5
14	30	4.62	105	1600	–	–	–	3.0	2.8	13.5 ± 0.4
15	0	3.64	75	1570	–	–	–	1.7	3.6	13.9 ± 0.4
16	0	4.62	75	1570	–	–	–	2.3	3.8	14.0 ± 0.6
17	0	4.13	120	1570	0	87.1	6.1	2.1	4.3	14.3 ± 0.6
18	0	4.13	90	1615	0	71.0	6.6	2.4	3.6	14.7 ± 0.9
19	30	3.64	105	1600	0	66.2	5.9	2.6	3.1	14.7 ± 0.7
20	30	4.13	60	1600	45.4	67.7	4.3	2.4	3.4	14.1 ± 0.6
21	30	4.13	90	1555	76.9	100.0	1.2	1.7	3.6	14.4 ± 0.9
22	0	4.13	90	1540	80.9	93.5	1.3	1.9	–	14.1 ± 1.2
23	0	4.13	90	1585	0	90.3	6.0	2.1	–	14.7 ± 0.5
24	0	4.13	90	1630	0	100.0	5.2	2.6	–	14.6 ± 0.6
25	15	7.89	90	1540	–	–	–	1.8	4.6	12.2 ± 0.8
26	15	7.89	90	1585	66.1	79.7	5.9	2.2	3.3	14.9 ± 0.9
27	15	7.89	90	1630	–	–	–	2.9	3.7	14.5 ± 0.8
29	*	4.13	90	1585	0	74.2	6.5	1.8	3.1	15.1 ± 0.8

that the phase $CaAl_{12}O_9$ could appear from the initial compositions in agreement with the quaternary Al_2O_3–MgO–CaO–SiO_2 diagram; but this phase has never been detected by XRD, so it was not taken into account in the calculations). The comparison between theoretical and experimental values evaluates the amount of vitreous phase in the intergranular phase. Then a glass coefficient $\Delta\alpha$ is obtained that gives comparative information for the different materials. For more details on this method please refer to.[7]

$$\Delta\alpha = \frac{M_{\text{anorthite}}^{\text{th}} + M_{\text{spinel}}^{\text{th}}}{M_{\text{alumina}}^{\text{th}}} - \frac{M_{\text{anorthite}}^{\text{XRD}} + M_{\text{spinel}}^{\text{XRD}}}{M_{\text{alumina}}^{\text{XRD}}} \quad (1)$$

with $M_{\text{phase}}^{\text{th}}$ the theoretical mass fraction of the considered phase deduced from the initial oxide content and $M_{\text{phase}}^{\text{XRD}}$ the mass fraction measured by X-ray diffraction.

The sintering additive contents are not the same in the different materials. Therefore, in order to compare them, a crystallization rate X_{phase} was calculated for each intergranular phase by dividing the actual measurement of mass fraction determined by X-ray diffraction by its theoretical value,

$$X_{\text{phase}} = \frac{M_{\text{phase}}^{\text{XRD}}}{M_{\text{phase}}^{\text{th}}} 100 \quad (2)$$

The total crystallization rate X_{total} was also calculated.

$$X_{\text{total}} = \frac{M_{\text{anorthite}}^{\text{th}} X_{\text{anorthite}} + M_{\text{spinel}}^{\text{th}} X_{\text{spinel}}}{M_{\text{anorthite}}^{\text{th}} + M_{\text{spinel}}^{\text{th}}} \quad (3)$$

The intergranular phases were also characterized by EDX for some TEM observations.

2.2.2. Dielectric measurements

The ability of an insulator to resist dielectric breakdown is defined by the breakdown strength E_b which is the maximum electrical field that can be applied without any degradation of the material. Bulk breakdown tests were performed on cylindrical samples of 20 mm in diameter. As the breakdown strength strongly depends on the sample thickness, all the samples were constructed to be uniform: to have the same thickness, approximately 3 mm. Liébault[4] determined the evolution law of E_b in the range of 0.7–3.5 mm for this type of materials. So, each value of E_b was calculated for a thickness of 3 mm exactly, from the expression:

$$E_b = \frac{V_b}{t} \sqrt{\frac{t}{3}}, \quad (4)$$

with V_b the voltage measured when breakdown occurs (kV) and t the sample thickness (mm). Thus, all E_b values are strictly comparable.
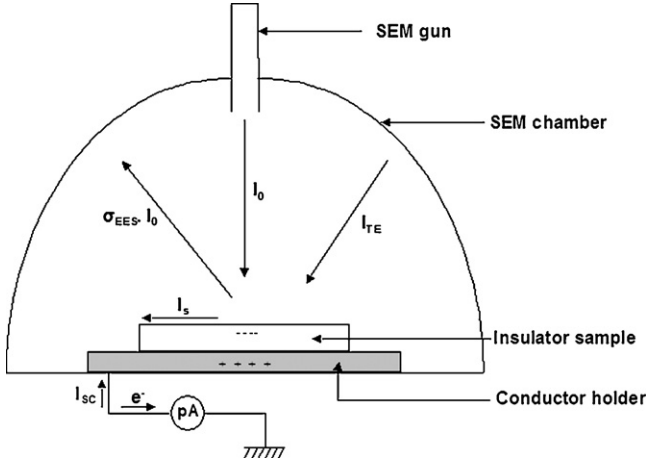
Fig. 1. Experimental set-up for ICM and SEMME measurements.

The test procedure must be precise enough to reduce the dispersion of E_b values. Specimens were tested directly after sintering to avoid acquiring surface impurities. Each sample was clamped between two hemispherical electrodes. The entire system was bathed in transformer oil to avoid flashover phenomena. After immersion, the oil bath was stirred with a magnet for 1 min to evacuate bubbles, and was then left untouched for another minute in order to stabilise the sample environment, before the voltage was applied. The dielectrimeter (Dieltest DTS-BAUR) operated on alternative current (50 Hz) at room temperature. The voltage rose at a rate of 1 kV/s until the insulator underwent catastrophic failure. Fifteen values of breakdown voltage were needed to have significant average breakdown strength E_b (kV/mm). These fifteen values were obtained by testing five specimens of each type at three separate locations for each specimen.

For high temperature measurements, a device, composed of a hermetically sealed quartz tube in which the sample is placed between two electrodes is used. The sample is a disc in which the center has been grounded to less than 600 μm. Before each test, the sample is heated to 350 °C in vacuum, and then cooled; the tube is then filled with a dielectric gas (SF$_6$). The rise in voltage is then applied until dielectric breakdown.

2.2.3. Charge transport and trapping characterizations

Electric charge transport and trapping properties have been investigated thanks to the Induced Current Measurement (ICM) and Scanning Electron Microscopy Mirror Effect (SEMME) methods allow to characterize material behaviour under electronic irradiation.[8–11] They give information on the ability of the insulator to carry and trap electric charges. These measurements are performed with a scanning electron microscope equipped with a beam blanking unit which permits an accurate check of the irradiation time, and a conductive cold-hot stage linked to the ground via a picoammeter. A schematic diagram of the experimental arrangement is shown in Fig. 1. The first step of the ICM and SEMME experiments is the injection of electrons into the sample during 100 ms. The impinging electron energy E_0 (30 keV) is so that the secondary emission yield stays at a value

lower than one. Thus, the implanted charge is negative and it produces positive "influence" charges in all conductive pieces of the SEM chamber (mainly in the holder). This "influence" charge is responsible of a current I_{SC} between the holder and the ground (electrons conducted through the insulator to the holder are negligible). Injected charge induces an electric field into the material and produces a negative surface potential that regulates the material behaviour toward the electron injection. The induced current is very sensitive to the insulator behaviour and is a function of

- the incident beam intensity I_0 ($I_0 = 3000$ pA);
- the secondary electron emission intensity $\sigma_{EES} \cdot I_0$ that corresponds to the electron emission from the insulator: impinging electron backscattering and secondary electron emission;
- the tertiary electron beam intensity I_{TE};
- the unsteady displacement current of polarization and trapping I_p;
- the surface spreading and leakage current I_s.

The intensity of the induced current, also named sample current I_{SC}, measured between the metallic sample holder and the ground is given by:

$$I_{SC} = (1 - \sigma_{EES}) \cdot I_0 + I_{TE} = I_p + I_{TE} + I_s \qquad (5)$$

Following this stage of electron injection, the SEM beam can be used as an electrostatic probe in the SEMME method. The acceleration voltage of the impinging electrons E_i (from 100 eV up to few keV) is then weaker than the surface potential V_0 (around −22 kV) induced by the charges stabilised during the e-injection. It is then possible, if the amount of stabilised charges is high enough, to observe a mirror effect. This effect is caused by the deflection of the impinging electrons by the potential field around the sample surface. The analysis of the mirror effect allows having access to the amount of stabilised trapped charges Q_t and the way they are distributed.

3. Results and discussion

3.1. Experimental design approach to establish elaboration conditions—dielectric breakdown resistance relationships

This first part presents curves in the form of "response surface" that describe a model of dielectric breakdown strength E_b evolution according to the elaboration parameters. This methodology[12,13] makes abstraction initially of samples microstructure and makes it possible to apprehend the sensitivity of this property E_b to the fluctuations of the elaboration conditions. This methodology has also the advantage to lead to a panel of different materials for the continuation of the study. Here, a simple empirical model was chosen: polynomial of the second order. The selected experimental design was of Doelhert type[13] with four factors. This type of experimental design makes it possible to model the evolution of a "response", here dielectric breakdown strength according to "variables", here elaboration parameters, thanks to a software called Nemrod®.[14]
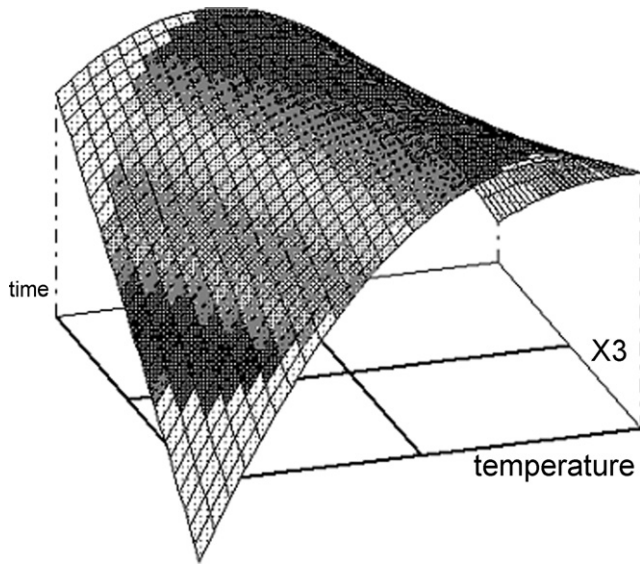
Fig. 2. Response surface of E_b versus soaking conditions (temperature and time); others parameters are at there median values: attrition time 15 min, additives content: 4.13 wt.%.

Four variables are considered, the "levels" are the following (the levels are the values of the parameters imposed by the experimental design):

- sintering aids contents considering the total oxides wt.% ($CaO + MgO + SiO_2$), 5 levels: 3.14; 3.64; 4.13; 4.62; 5.10%,
- attrition time, 3 levels: 0, 15 and 30 min,
- sintering soaking time, 7 levels: 45; 60; 75; 90; 105; 120; 135 min,
- sintering soaking temperature, 7 levels: 1540; 1555; 1570; 1585; 1600; 1615; 1640 °C.

The Doëhlert experimental design is described in Table 3: each row corresponds to an experiment, while each column corresponds to a variable (except the last one where the response E_b at 25 °C obtained for each experiment is reported).

Before the establishment of the curves, the validity of the model was verified: values of residue (difference between experimental and computed values according to the model) make it possible to validate the model, because they vary in the range 0.001–0.47 kV/mm. Indeed, these residues are comparable with the values of standard deviation. The residues are higher on the board than inside the field. It is thus necessary to consider the results given by the model beyond the limits of the field carefully.

The response surface (Fig. 2) shows a plateau of dielectric breakdown strength values. The two zones of low values of E_b correspond to conditions where one can encounter problems of sintering. In the zone of low temperature and short soaking, densification could be still not achieved, whereas in the zone of high temperature—long soaking times, there could be a risk of grain coarsening.

E_b is not very sensitive to the sintering aids content whereas the attrition duration seems to have more influence (Fig. 3): in the case of a non-milled powder, the highest values of rigidity are obtained for short times and high sintering temperatures whereas
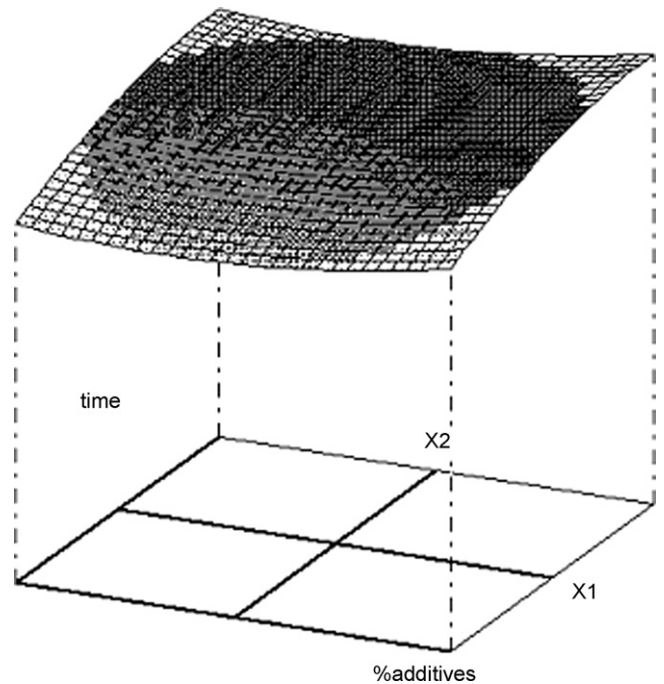

Fig. 3. Response surface of E_b versus attrition time and sintering aids content; other parameters are at their median values: soaking temperature: 1585 °C, and time: 90 min.

in the case of a milled powder (30 min), it is for long soaking times and low temperatures that the materials present the best resistance to dielectric breakdown at room temperature.

This analysis shows that the sintering parameters are those which have the greatest influence on dielectric breakdown strength and that light fluctuations of the additives contents or attrition milling of the powder have less incidence. Beyond this first analysis, a finer understanding of the role of the microstructure on dielectric breakdown strength appears necessary in order to point out the influence of porosity, grain size and intergranular phase. Indeed, the plateau observed in Fig. 3 could be due to balance effects of these parameters.

3.2. Dielectric breakdown strength—microstructure parameters relationships

In order to establish relationships between microstructure parameters and dielectric breakdown strength, the panel of material was completed and samples were analysed; results are presented in Table 2.

3.2.1. At room temperature
3.2.1.1. Effect of porosity. As shown by Liébault,[15] for sintered alumina materials, a porosity rate below 5% has no significant effect on breakdown strength. In this work, since almost all the sintered materials present a porosity around 3–4%, we ignore porosity as a parameter on the breakdown strength. The three samples that present a higher porosity rate (>4.5%) correspond to low E_b values; this is in agreement with Liébault's results.

3.2.1.2. Effect of grain size. During sintering, the different oxides react together to form intergranular phase. These reac-

Table 3
Doëhlert experimental design and dielectric breakdown resistance E_b at 25 °C.

Experiment no.	Attrition milling time (min)	Additives (wt. %)	Sintering conditions		E_b (kV/mm)
			Soaking time (min)	Soaking temperature (°C)	
1	15	4.13	90	1585	14.3 ± 0.4
2	15	5.10	90	1585	14.5 ± 0.8
3	15	3.14	90	1585	14.3 ± 0.6
4	15	4.62	135	1585	14.3 ± 0.4
5	15	3.64	45	1585	14.2 ± 0.9
6	15	4.62	45	1585	14.2 ± 0.9
7	15	3.64	135	1585	14.3 ± 0.6
8	15	4.62	105	1630	13.7 ± 0.5
9	15	3.64	75	1540	12.0 ± 2.6
10	15	4.62	75	1540	13.3 ± 0.8
11	15	4.13	120	1540	14.0 ± 0.9
12	15	3.64	105	1630	13.6 ± 0.6
13	15	4.13	60	1630	13.9 ± 0.5
14	30	4.62	105	1600	13.5 ± 0.4
15	0	3.64	75	1570	13.9 ± 0.4
16	0	4.62	75	1570	14.0 ± 0.6
17	0	4.13	120	1570	14.3 ± 0.6
18	0	4.13	90	1615	14.7 ± 0.9
19	30	3.64	105	1600	14.7 ± 0.7
20	30	4.13	60	1600	14.1 ± 0.6
21	30	4.13	90	1555	14.4 ± 0.9

tions will be detailed in Section 2.3 : spinel ($MgAl_2O_4$) and anorthite ($CaAl_2Si_2O_8$) are formed at grain boundaries after sintering. Focusing on the crystallization rate mentioned in Table 2, three classes of materials are distinguished according to the glass coefficient $\Delta\alpha$ which is directly linked to the amount of vitreous phase inside the grain boundaries. These materials present:

- a highly crystallized intergranular phase ($\Delta\alpha < 5$),
- an intermediately crystallized intergranular phase ($5 < \Delta\alpha < 7$),
- a preferentially vitreous secondary phase ($\Delta\alpha > 7$).

This classification differentiates the effects due to the interface density (average grain diameter) and those due to the interface nature (intergranular phase composition).

Fig. 4 shows the breakdown strength E_b as a function of the average grain diameter at room temperature for the intermediate crystallization rate, for which the number of samples is high.

This figure shows that the breakdown strength decreases when the average grain size increases. These results can be interpreted in term of interface density. Indeed, the increase in average grain diameter which is detrimental to the dielectric breakdown resistance is directly linked to interface density. The higher the average grain size, the lower the interface density, and so the lower the dielectric breakdown resistance.

3.2.1.3. *Effect of intergranular phase.* The average E_b for the three *classes* of material defined above are compared, for materials with comparable grain size (from 2 to 2.5 μm):

- highly crystallized intergranular phase ($\Delta\alpha < 5$): $E_b = 14.2$ kV/mm,

- intermediately crystallized intergranular phase ($5 < \Delta\alpha < 7$): $E_b = 14.8$ kV/mm,
- preferentially vitreous secondary phase ($\Delta\alpha > 7$): $E_b = 14.5$ kV/mm.

The influence of crystallized phase is not so obvious, but it seems that a high content of anorthite does not favor breakdown resistance at room temperature.

Indeed, the nature of the intergranular phase could also plays a role on the interface density and we can make the assumption that for a given grain size, materials which present simultaneously a vitreous phase and various crystallized phases could be the richest in interfaces. Those containing more anorthite crystals are poorer in interfaces (the TEM analysis showed that anorthite
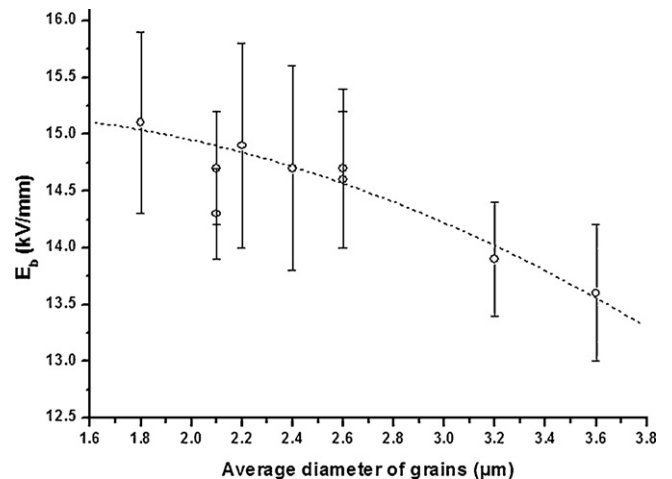

Fig. 4. Breakdown strength E_b at room temperature as a function of the grain size for materials presenting an intermediate crystallization rate ($5 < \Delta\alpha < 7$).
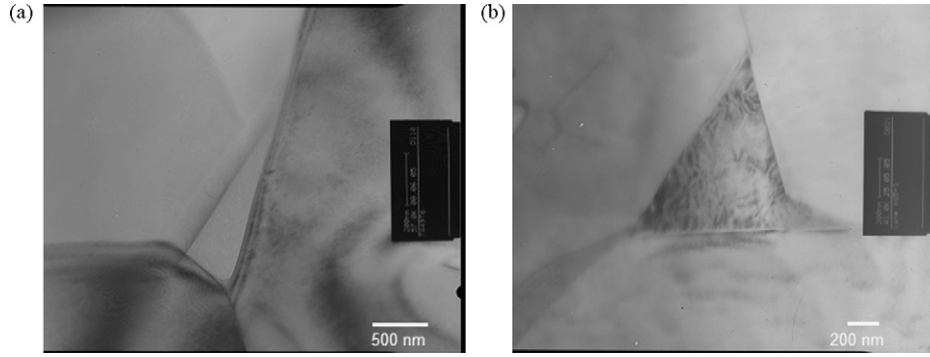
Fig. 5. TEM observations of (a) a vitreous triple point (white triangle) in material 4 (its composition is close to that of anorthite) and (b) an anorthite crystallized triple point (grey speckled) in material 26.

crystals are not mixed with glass, but fill the triple point, see Fig. 5b). The poorest materials in interfaces would be then those which present a very glass rich intergranular phase.

3.2.2. At higher temperature $(25\,°C < T < 250\,°C)$

The dielectric breakdown strength E_b was measured at different temperatures up to 250 °C for the materials 26 and 29. They were chosen because both attain the highest Ec at room temperature (14.9 kV/mm for 26 and 15.1 kV/mm for 29). As shown in Table 2, they present a similar grain size (2.2 μm for 26, 1.8 μm for 29) and glass ratio in the intergranular phase (5.9 for 26 and 6.4 for 29). Thanks to these analogous characteristics, one can assume that the interface densities are nearly the same for both materials. However, the nature of their interfaces is different: material 26 contains anorthite crystals, that lead to alumina–anorthite and glass–anorthite interfaces which do not exist in 29. The E_b progression versus temperature up to 250 °C (Fig. 6) shows that in the intermediate temperature range (50–120 °C) the values are slightly lower than those obtained at room temperature for both materials. For the upper temperatures (250 °C), the two materials differ greatly: the resistance of material 29 (presence of vitreous phase in grain boundaries) is the same as that obtained at room temperature, while E_b decreases down to 9 kV/mm for material presenting anorthite in the intergranular phase (26).
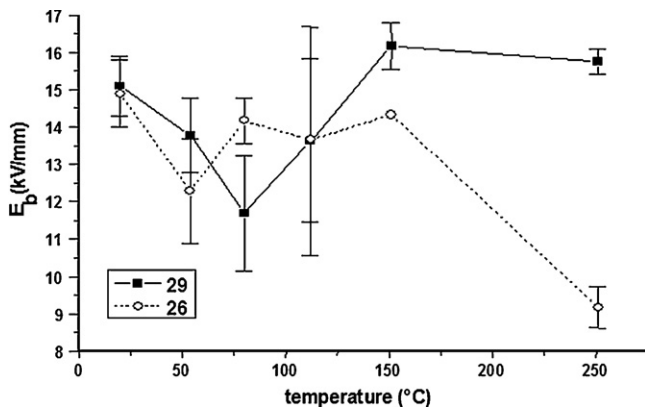

Fig. 6. Breakdown strength versus temperature for materials 26 (with anorthite crystals) and 29 (without anorthite crystals).

This difference underlines the role of the composition of the interface on charge transport, and consequently on the dielectric breakdown at high temperature.

3.2.3. Charge transport measurements; how charge transport can explain breakdown strength resistance?

Trapped charge measurements with the SEMME method on a selection of these alumina materials has been described before,[16] these results are first briefly summarized in this part. The SEMME permits to know a posteriori the amount of stabilised trapped charge. But, for a better understanding of charge trapping and transport, it is useful to complete these results by the curves obtained thanks to the Induced Current Method, which is a dynamic measurement during the e-injection. The results of both methods are then connected with the breakdown resistance and microstructures of alumina materials.

Choice of the materials 4, 1, 29 and 26: After sintering, materials **4, 1, 29** exhibit a mainly vitreous intergranular phase (intergranular phase crystallization rate lower than 30%) with a small amount of spinel phase ($MgAl_2O_4$, <3 wt.%). These three materials mainly differ by the average grain size which decreases for the materials as follow **4 > 1 > 29**. In material 26 grain boundaries are quite different from those of the other materials since they are much more crystallized (intergranular phase crystallization rate greater than 70%) into anorthite phase ($CaAl_2Si_2O_8$, 6.4 wt.%) and spinel phase ($MgAl_2O_4$, 4.7 wt.%). These microstructural parameters can be interpreted in terms of interface density and nature. Indeed, grain boundaries lead to different kind of interfaces: alumina–glass, alumina–anorthite and alumina–spinel. Thus, interface density increases for the materials as follow **4 < 1 < 29**. The interface nature is almost the same for these three materials (essentially alumina–glass). Because of its high secondary phase crystallization rate, material 26 presents an additional type of interfaces: alumina–anorthite. Interface nature and density have a great influence on charge transport properties. Indeed, electric charge trapping in insulator materials can be attributed to different kind of defects; point defects (vacancies, interstitial sites ...),[17] linear defects (dislocations ...) or interfaces (grain boundaries, interphases ...). These defects induce permittivity variation of the medium leading to the trapping of charges.
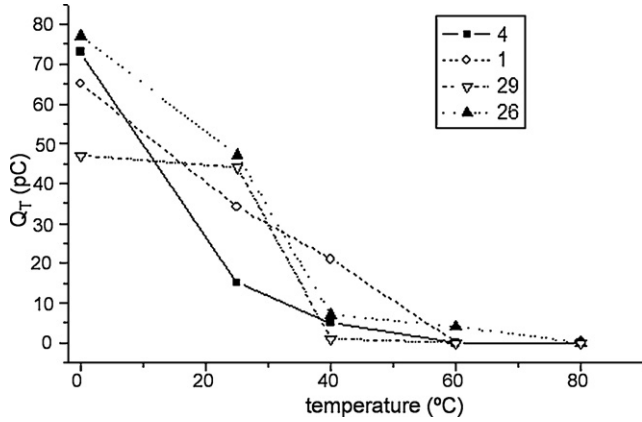
Fig. 7. Stabilised trapped charge amount Q_t as a function of the temperature for the four materials 4, 1, 29 and 26—injected charge amount $Q_i = 300$ Pc.

3.2.3.1. At room temperature.

3.2.3.1. At room temperature. Dielectric breakdown strength E_b as a function of the amount of trapped charge after electron bombardment Q_t at room temperature was described in[16] for different materials. At room temperature, all the tested materials exhibited high stabilised trapped charge amount Q_t. However, this quantity depended on the considered material. Indeed, the higher the interface density, the higher the trapped charge amount Q_t; this was obtained for material with low grain size, and/or a high amount of anorthite.

The relation between E_b and the Q_t was also described and it was shown that high stabilised charge is connected to high resistance to dielectric breakdown: so the ability of materials to stabilise a great amount of charge leads to an improvement of the resistance to breakdown, probably because this great amount of stored charges prevents further charge injection.

3.2.3.2. At higher temperature. The evolution of the amount of trapped charge Q_t as a function of the temperature has been measured by the SEMME method was also described in.[16] The results, which are presented in Fig. 7 give information on the depth of the different trapping sites for four materials.

As it can be seen on this figure, temperature has a great impact on the charge trapping phenomenon. Indeed, an increase of the temperature, even from 40 °C, leads to a huge decrease of the amount of trapped charge stabilised after irradiation. At 60 °C, material 26 is the only one that exhibits a stabilised trapped charge amount different from zero. Beyond 80 °C, there is no more visible mirror effect for any materials, meaning that not enough charges are strongly stabilised. The temperature increase leads to the decrease of the effective depth of the traps. The complexity of the grain boundary structure and composition of the materials considered in this work makes it difficult to establish quantitative correlation between grain boundary properties and the ability of the material to trap charges. However, it is possible to point out qualitative correlation. Thus, traps due to the presence of anorthite crystals at grain boundaries seem to be deeper than those due to the glassy phase. Indeed, material 26, which differs from the other materials by a more crystallized intergranular phase (anorthite crystals), is the only one to still exhibit a mirror effect at 60 °C. On the contrary, the vitreous phase seems

to improve the spreading of charges in the material when temperature increases. This phenomenon can be attributed to the atomic disorder introduced by this phase which creates localised electronic states at the edge of the conduction band. These localised states can lead to thermal activated conduction phenomena.[18]

The four materials were then tested with the ICM method (see Section 2.2.3) at different temperatures to better understand the behaviour under charge injection. However previously to compare the various behaviours under e-injection, it is useful to understand the general shape of the induced current I_{SC}.

In order to interpret the ICM measurements, a numerical simulation of the electron beam charging of insulators has been performed. In this simulation, tertiary electrons are not taken into account and leakage surface current is not integrated in the sample current as it is the case in the ICM measurements. For more details on this simulation please refer to.[19–21] In spite of these restrictions, the general form of the ICM curves can be however qualitatively interpreted and the charging regulation mechanism pointed out. Fig. 8a shows a typical simulated J_{SC} current density curve obtained on alumina at room temperature during electron injection and the simultaneous variation of the surface potential. At the beginning of the electron injection, the sample current is positive meaning that the injected charge becomes more and more negative. This negative charge generates a negative surface potential which deflects and decelerates the electron beam. The surface potential increase leads to the increase of the secondary electron emission rate and leakage current. Thus, the total implanted charge increases less quickly. That corresponds to a decrease of the sample current. Then, the current reaches the value of zero meaning that the total implanted charge does not evolve further, the system has reached equilibrium between injection and evacuation of charges. In case of the presence of a leakage current the steady-state current value will not be zero.

Fig. 8b shows the experimental currents versus injection time, at 20, 40, 60 and 80 °C, for the material 29, and can be compared with the simulated curve. The experimental curves present higher values of current than those calculated from the numerical simulation. This difference can be connected to additional currents included in the measured sample current I_{SC}; these currents are mainly due to tertiary electrons, which come from the collisions of the secondary electrons on the walls of the microscope chamber, then return on the sample surface. The quantitative analysis of the experimental curves is thus difficult, but qualitative comparisons are possible: at 20 °C, the sample current I_{SC} decreases during the whole injection process. At this temperature, the material durably traps charges and the negative slope for the current until the end of injection is due to the increase of the secondary electron emission; this strong emission rate can be connected with a high surface potential.

The transition between a trapping behaviour and a diffusion one takes place between 20 and 40 °C. For the temperatures of 40 °C and upper, I_{SC} curves take a different shape: they first fall because of the building of a negative potential, then the slope is reversed and the value of the sample current increases again. The rise in the temperature leads to the increase in the evacuation of the charges by material thanks to surface diffusion current.[21] The
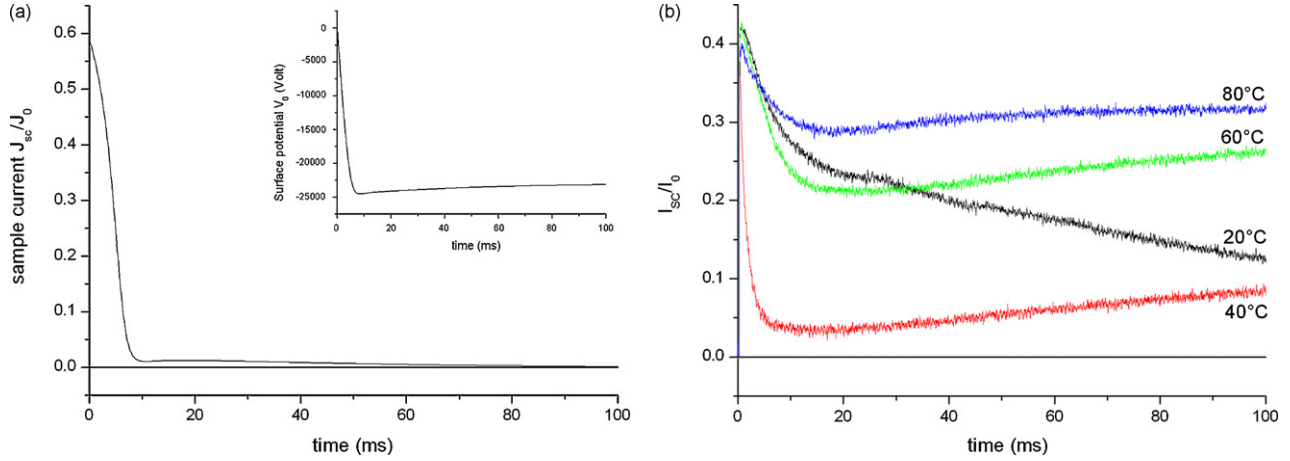
Fig. 8. Evolution of the sample current I_{SC} as a function of irradiation time for the material 29: simulated curve with the simultaneous variation of the surface potential (a) and influence of the temperature on I_{SC} experimental curves (b).

lateral diffusion of the charges due to the electrostatic repulsions between them,[1] as well as the positive electric field in this zone of material,[20] lead to a spreading out of the electrons by the surface of insulator. Thus, the increase of the temperature leads to the increase of charge detrapping phenomena. As a result, charges are more mobile and the surface current increases.

Fig. 9 makes it possible to compare for four temperatures the influence of the microstructure on the establishment of a steady-state evacuation current during the injection.

The curves carried out at 20 °C show, for all the materials, a charge trapping behaviour. Indeed, the current decreases during the whole electron injection procedure as previously said this strong emission rate can be connected with a high surface potential.

From 40 °C, two behaviours can be distinguished. Thus, materials 1 and 26 continue to present typical curves of trapping behaviour whereas the curves corresponding to materials 4 and 29 indicate the appearance of a diffusion current (increase of the induced sample current during electron injection). At 60 °C, only the I_{SC} measured for the material 26 decreases during the whole injection procedure, while those corresponding to the three other materials indicate a charge diffusion behaviour. At 80 °C, the four curves correspond to a diffusion behaviour. These observations are in agreement with measurements of the trapped charge amount performed by mirror effect method. The microstructure influences the behaviour of materials in terms of charge transport and trapping. On the one hand, the material which adopts a charge diffusion behaviour at the highest temperature is the material 26. This material presents a very crystallized intergranular phase which enhances the trapping of charge. On the other hand, materials 4 and 29 adopt a charge diffusion behaviour at lower temperature (40 °C). The microstructure of these materials is characterized by a very poorly crystallized intergranular phase which makes the diffusion of charges much easier even at relatively low temperatures.

These results are in agreement with the work of BRAGA[22] who studied charge injection and transport phenomena in insulating materials subjected to a low energy electron beam (200 eV to 30 keV) at room temperature. He thus showed that one could classify insulators according to two categories considering their capacity to release the generated charges: "trapping insulators" which are able to keep charges stabilised during long time and the "conductive insulators" which more or less quickly release charges according to their density and their mobility. It was thus highlighted, in the case of "conductive" insulators, the existence of a steady-state current which makes it possible to control the charge density in the material. The present work thus permits to point out on the one hand the influence of the microstructure, at room temperature, on the "trapping" or "conductive" character (by taking again the terms of BRAGA) of an insulator, and on the other hand the transition between these two characters when the temperature increases with the establishment of a steady-state current making it possible to evacuate charges via the insulator surface.

By considering this classification, two breakdown resistance mechanisms, and the corresponding microstructure, depending on the temperature can be highlighted. Up to 80 °C, the dielectric strength is improved by high trapped charge stabilisation ability. That is connected to high grain boundary density (fine grain size) and crystallized intergranular phase. On the contrary, at higher temperature, the spreading of charges permits to delay breakdown phenomenon. This behaviour is improved by vitreous grain boundaries.

3.3. Elaboration—microstructure parameters relationships: how to obtain a microstructure favorable to high E_b?

From previous and present study, it is known that breakdown resistance is improved when porosity is less than 5 vol.% and grain size is low: it is well known that this is obtained by starting from fine grain alumina (ex: material 29), by the control of the sintering conditions (ex: temperature high enough to promote densification, but not too high to avoid grain coarsening) . . . In this part, we will focus on the control of intergranular phases, particularly the crystallization of anorthite at grain boundaries which influences strongly E_b at high temperature as described above.
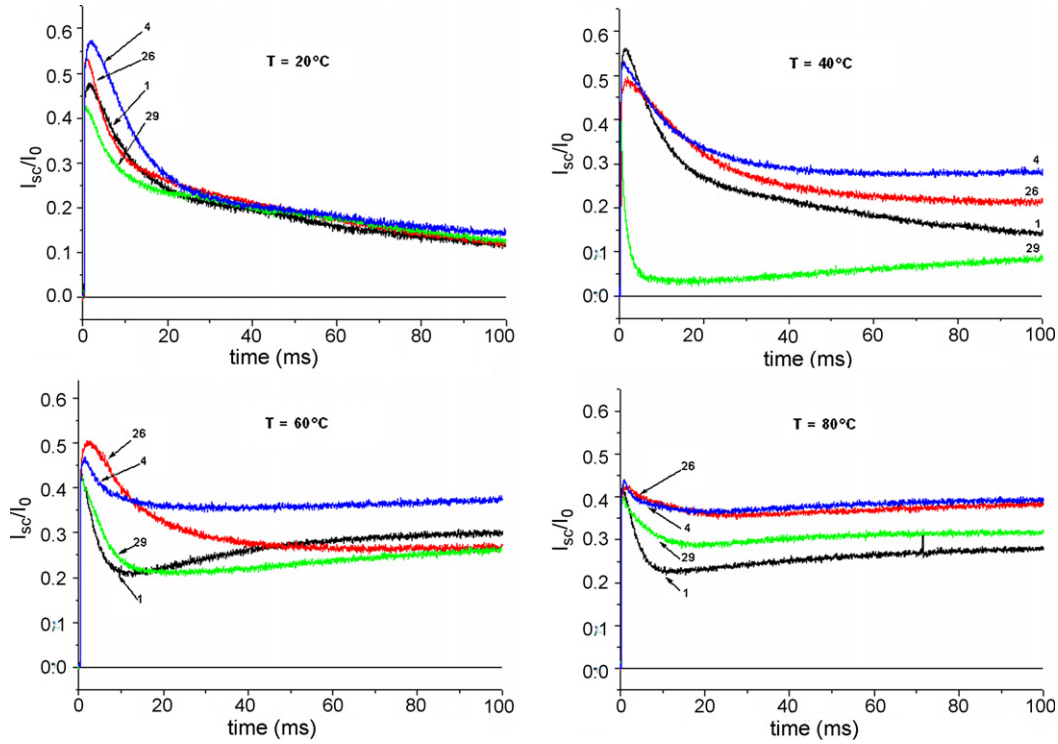
Fig. 9. Evolution of the induced sample current I_{SC} as a function of irradiation time for the four materials 4, 1, 29 and 26 at different temperatures.

As mentioned above, during sintering, the different oxides (Al_2O_3, CaO, MgO and SiO_2) react together to form different intergranular phases. These phases can be formed either in solid or in liquid phase during heating or cooling. X-ray diffraction patterns show the presence of three crystallized phases: alumina (Al_2O_3), spinel ($MgAl_2O_4$) and anorthite ($CaAl_2Si_2O_8$). More-over, it is certain that the different oxides also take part to the formation of a vitreous phase at the grain boundaries.

By using the method described in Section 2.2, crystallization rate X_{phase} has been calculated for each intergranular phase. Results are given in Table 2: the spinel phase is detected for all tested materials. Its crystallization rate is always greater than 60% of the theoretical value and reaches 100% for some cases. This indicates that the main part of MgO which comes from the initial mineral additives leads to the formation of the spinel phase $MgAl_2O_4$. However, the anorthite phase is detected only in some materials (11, 20, 21, 22, 25, and 26). The glass coefficient $\Delta\alpha$ which is function of the quantity of the vitreous phase in grain boundaries varies greatly in magnitude (from 0.5 to 8). Actually, materials 11, 21 and 22 present a very low coefficient $\Delta\alpha$, meaning that they contain a very small amount of non-crystallized phase whereas materials 1, 2, 4, 8, 12, 17, 18, 23 and 29 are those which contain the great amount of vitreous phase. The crystallization rate of the anorthite phase $X_{anorthite}$ as a function of sintering temperature is presented in Fig. 10.

Except for materials 20 and 26, the anorthite crystallization seems to be very dependent on the sintering temperature. Indeed, up to 1555 °C the crystallization rate of anorthite is greater than 60% of the theoretical value. Beyond this temperature, this phase is no longer detected. In order to understand the formation of the

different crystallized phases and to interpret the evolution of the intergranular phase composition as a function of the elaboration parameters, pellets of the powder containing 7.89% sintering additives (15 min attrition milling) were heated at different temperatures for a short time (10 min). Then, they were quenched at room temperature, and characterized by X-ray diffraction. The corresponding crystallization rate evolution of the spinel and anorthite phases is given in Fig. 11.

During the heating, CaO, MgO and SiO_2 react together to form an enstatite phase ($MgO \cdot SiO_2$) around 1100 °C, and prob-ably some amorphous phases containing Ca. At 1325 °C, the disappearance of this phase corresponds to the formation of the
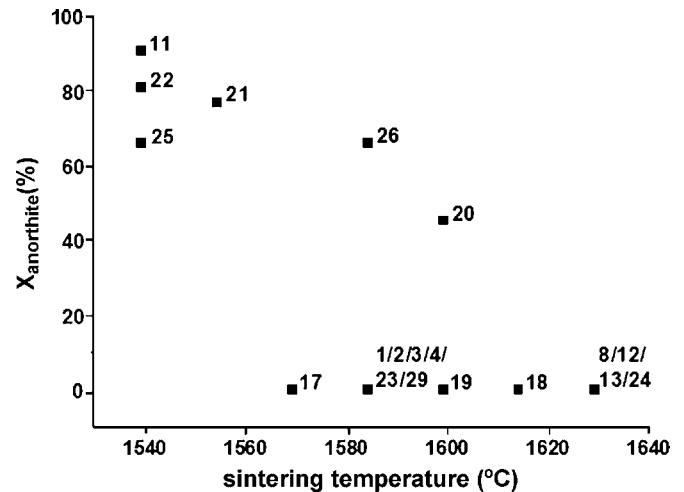

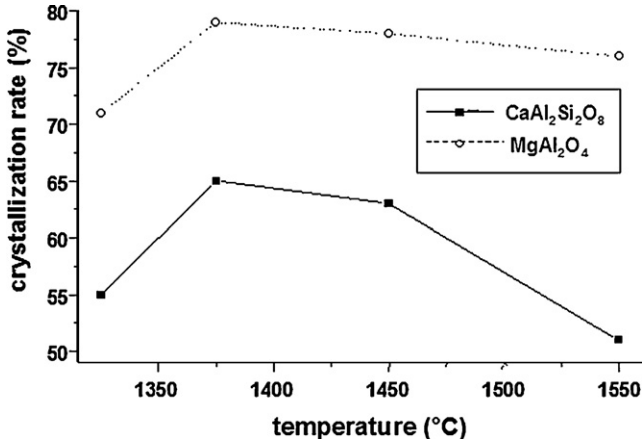Fig. 10. Crystallization rate of anorthite $X_{anorthite}$ as a function of the sintering temperature.

Fig. 11. Crystallization rate evolution of the spinel and anorthite phases during the heating.

spinel ($MgO \cdot Al_2O_3$) and anorthite ($CaO \cdot Al_2O_3 \cdot 2SiO_2$) phases. The crystallization of both phases keeps on increasing up to 1375 °C and then stabilises at 1450 °C. Beyond 1550 °C, the crystallization of the anorthite phase abruptly decreases while the spinel phase stays constant. For all materials, the crystallization rate in the spinel phase is greater than 60%. Moreover, it is known that this phase has a very low solubility in the liquid Al_2O_3–CaO–SiO_2.[23] So it is reasonable to make the assumption

that the liquid phase composition moves mainly in the ternary diagram Al_2O_3–CaO–SiO_2 (Fig. 12).

Indeed, as illustrated in Fig. 12, we can consider that the composition of the liquid moves along the line joining the alumina pole to the point located on the SiO_2–CaO line. This point corresponds to the proportion of these two oxides in the starting powders. The amount of Al_2O_3 in the intergranular phase before sintering is unknown. However, by considering the initial CaO/SiO_2 ratio, the starting composition can be assumed to be close to that of the anorthite. During the heating, due to the fine Al_2O_3 grains dissolution in the liquid, the composition of the intergranular phase moves along the line in direction of the alumina pole. As afore mentioned, the formation of anorthite during the heating pointed out previously is in accordance with the ternary phase diagram. Notice in Fig. 12, that beyond 1553 °C, the anorthite phase is completely melted. This explains the decrease of the crystallization rate of the anorthite observed at 1550 °C in Fig. 11. At this temperature, the secondary phase is essentially liquid and can then dissolve fine alumina crystals. The composition of the intergranular phase continues to move into the ternary diagram in direction of the Al_2O_3 pole. Because of this enrichment in alumina, the liquid solidifies both via the precipitation of alumina as well as the formation of a glassy phase.[25,26] This is why the majority of materials sintered beyond the melting temperature of anorthite (1553 °C) does not contain any anorthite crystals but a vitreous phase. As it has been described previously, two materials (20 and 26) show the pres-

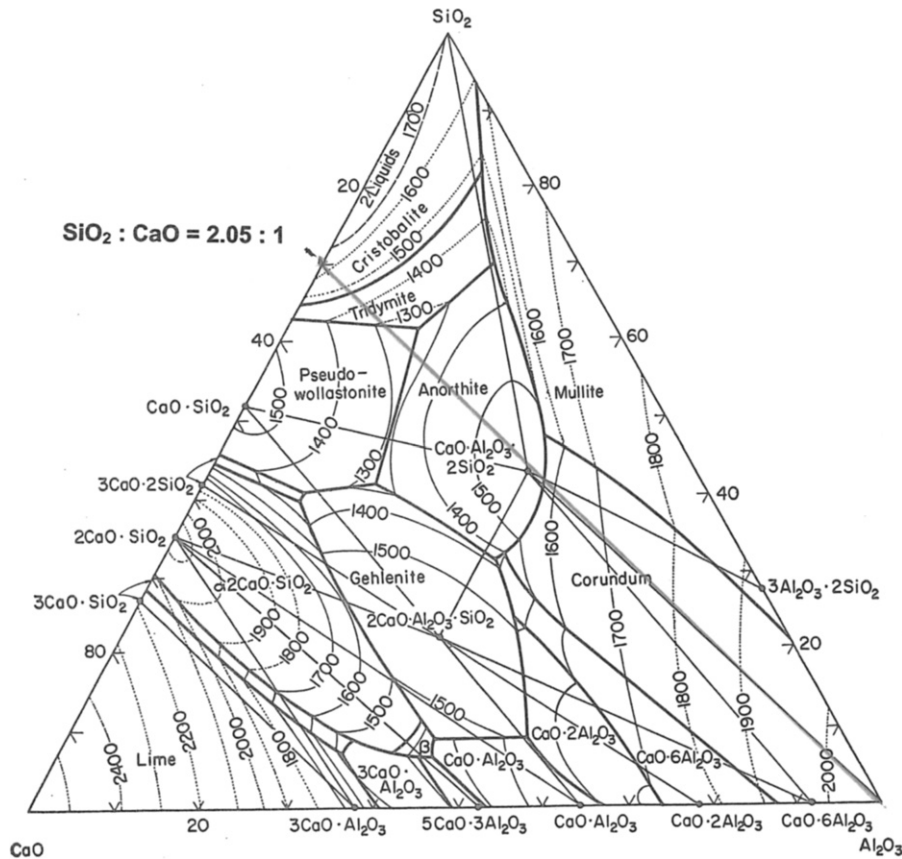Fig. 12. Phase diagram of the ternary system Al_2O_3–CaO–SiO_2.[24]

ence of anorthite phase within the intergranular phase although they have been sintered beyond 1550 °C. Material 20 is characterized by a short soaking time (60 min) and material 26 by a high sintering additive content (7.89%). These conditions lead to a weaker alumina enrichment of the intergranular phase and thus a weaker displacement in the ternary diagram. In this case, the liquid composition remains in the anorthite domain and crystallizes during the cooling. This assumption is confirmed by the TEM observations performed on materials 4 and 26 represented in Fig. 5a and b.

In conclusion, many factors influence the formation of anorthite crystals in such a system: alumina grain size, additions contents, soaking time and temperature during sintering. Other parameters have also an influence that is not described here: cooling rate for example; and some annealing treatments after sintering permit also to modify the crystallization of anorthite . . .

4. Conclusion

Alumina materials sintered with liquid phase thanks to sintering aids containing SiO_2, CaO and MgO present various microstructures in terms of porosity, grain size and nature of the intergranular phase that depend on the elaboration process (raw alumina grain size, composition, sintering conditions . . .). The dielectric breakdown strength E_b measurements for different materials in this system make it possible to highlight the great influence of the microstructure parameters. Those, like the grain size and the composition of intergranular phase have a direct impact on the density and the nature of interfaces. These influences of the microstructure can be linked to the trapping-transport behaviour under e-injection described above.

The main results are:

- at room temperature, one way to avoid breakdown is to prevent charge injection, by a high trapping at the beginning of the e-injection that leads to a high local potential that stop further injection. That explains why the higher interface density, and so the higher trap density leads to the higher dielectric breakdown resistance E_b at room temperature;
- on the contrary, at high temperature, we demonstrated that breakdown resistance is stronger when charges can be evacuated from the injection area. The presence of anorthite in the intergranular phase is not favorable to E_b at high temperature. This can be explained by the e-injection study which showed that the presence of anorthite leads to deeper traps and so to a trapping behaviour even at high temperature. Moreover, the charge evacuation is enhanced by highly vitreous grain boundaries.

References

1. Blaise, G. and Le Gressus, C., Charging and flashover induced by surface polarization relaxation process. *J. Appl. Phys.*, 1991, **69**, 6334–6339.

2. Blaise, G. and Le Gressus, C., Mise en évidence d'un claquage des isolants associé à la déstabilisation d'une charge d'espace localisée. *C.R. Acad. Sci. Paris*, 1992, **t314**, 1017–1024.

3. Will, F. G., Delorenzi, H. G. and Janora, K. H., Conduction mechanism of single-crystal alumina. *J. Am. Ceram. Soc.*, 1992, **75**, 295.

4. Liébault, J., Vallayer, J., Goeuriot, D., Tréheux, D. and Thévenot, F., How the trapping of charges can explain the dielectric performance of alumina ceramics. *J. Eur. Ceram. Soc.*, 2001, **21**, 389–397.

5. Si Ahmed, A., Kansky, J., Zarbout, K., Moya, G., Liébault, J. and Goeuriot, D., Microstructural origin of the dielectric breakdown strength in alumina: a study by positron lifetime spectroscopy. *J. Eur. Ceram. Soc.*, 2005, **25**, 2813–2816.

6. Kolk, J. and Heasell, E. L., A study of charge trapping in the Al-Al_2O_3-Si MIS system. *Solid-State Electron.*, 1980, **23**, 101–107.

7. Touzin, M., PhD Thesis. 384SGM. Saint-Etienne, France, 2005.

8. Vallayer, B., Blaise, G. and Tréheux, D., Space charge measurement in a dielectric material after irradiation with a 30 kV electron beam application to single-crystal oxide trapping properties. *Rev. Sci. Instrum.*, 1999, **70**, 3102–3112.

9. Wintle, H. J., Analysis of the scanning electron microscope mirror method for studying space charge insulators. *J. Appl. Phys.*, 1999, **86**, 5961–5967.

10. Jbara, O., Belhaj, M., Odof, K., Msellak, K., Rau, E. I. and Andrianov, M. V., Surface potential measurements of electron-irradiated insulators using backscattered and secondary electron spectra from an electrostatic torroidal spectrometer adapted for scanning electron microscope applications. *Rev. Sci. Instrum.*, 2001, **72**, 1788–1795.

11. Bigarré, J., Attard, C., Hourquebie, P. and Matallana, J., SEM-mirror methods and application to insulator characterization. *IEEE Trans. Electron. Insul.*, 2001, **8**, 942–952.

12. Ficarra, R., Cutroneo, P., Aturki, Z., Tommasini, S., Calabrò, M. L., Phan-Tan-Luu, R. *et al.*, An experimental design methodology applied to the enantioseparation of a non-steroidal anti-inflammatory drug candidate. *J. Pharm. Biomed. Anal.*, 2002, **2–6**, 989–997.

13. Zolgharnein, J., Shahmoradi, A. and Sangi, M. R., Optimization of Pb(II) biosorption by Robinia tree leaves using statistical design of experiments. *Talanta*, 2008, **76**, 528–532.

14. Mathieu, D., Phan-Tan-Luu, R. Nemrod®, LPRAI SARL. Marseille, F-13331, France.

15. Liébault, J., PhD Thesis. 206TD. Saint-Etienne, France, 1999.

16. Touzin, M., Goeuriot, D., Fitting, H. J., Guerret-Piécourt, C., Juvé, D. and Tréheux, D., Relationships between dielectric breakdown resistance and charge transport in alumina materials—effects of microstructure. *J. Eur. Ceram. Soc.*, 2007, **27**, 1193–1197.

17. Jacobs, P. W. M. and Kotomin, E. A., Theory of point defect and vacancy motion in corundum crystals. *J. Sol. State Chem.*, 1993, **106**, 27–34.

18. Blaise, G., Charge localization and transport in disordered dielectric materials. *J. Electrostat.*, 2001, **50**, 69–89.

19. Meyza, X., Goeuriot, D., Guerret-Piécourt, C., Tréheux, D. and Fitting, H.-J., Secondary electron emission and self-consistent charge transport and storage in bulk insulators: application to alumina. *J. Appl. Phys.*, 2003, **94**, 5384–5392.

20. Touzin, M., Goeuriot, D., Guerret-Piécourt, C., Juvé, D., Tréheux, D. and Fitting, H.-J., Electron beam charging of insulators: a self-consistent flight-drift model. *J. Appl. Phys.*, 2006, **99**, 114110–114123.

21. Cornet, N., Goeuriot, D., Guerret-Piécourt, C., Juvé, D., Tréheux, D., Touzin, M. *et al.*, Electron beam charging of insulators with surface layer and leakage currents. *J. Appl. Phys.*, 2008, 103.

22. Braga, G., *Etude des phénomènes de charge des matériaux isolants sous faisceau d'électrons de basse énergie (200 eV–30 keV)*. PhD Thesis. Université Paris XI, Orsay, 2003.

23. De Aza, A. H., Iglesias, J. E., Pena, P. and De Aza, S., Ternary System Al_2O_3-MgO-CaO: II, phase relationships in the subsystem Al_2O_3-$MgAl_2O_4$-$CaAl_4O_7$. *J. Am. Ceram. Soc.*, 2000, **83**(4), 919–927.

24. Levin, E. M., Robbins, C. R. and McMurdie, H. F., *Phase Diagram for Ceramists* (*1st ed.*). The American Ceramic Society Inc., 1964.

25. Brydson, R., Chen, S. C., Riley, F. L. and Milne, S. J., Microstructure and chemistry of intergranular glassy films in liquid-phase-sintered alumina. *J. Am. Ceram. Soc.*, 1998, **81**(2), 369–379.

26. Vasquez, B. A., Caballero, A. and Pena, P., Quaternary system Al_2O_3-CaO-MgO-SiO_2: I, study of the crystallisation volume of Al_2O_3. *J. Am. Ceram. Soc.*, 2003, **86**(12), 2195–2199;
Vasquez, B. A., Caballero, A. and Pena, P., Quaternary system Al_2O_3-CaO-MgO-SiO_2: II, study of the crystallisation volume of Mg Al_2O_4. *J. Am. Ceram. Soc.*, 2005, **88**(7), 1949–1957.